JOURNAL OF AIRCRAFT
Vol. 47, No. 6, November–December 2010

Optimizing Spanwise Lift Distributions Yacht Sails Using Extended Lifting Line Analysis

Timm Junge,* Frederik C. Gerhardt,† Peter Richards,‡ and Richard G. J. Flay§
University of Auckland, Auckland 1142, New Zealand

DOI: 10.2514/1.C001011

This paper discusses how to maximize the drive force produced by an upwind sail. It aims to provide a better understanding of the behavior of this force as a function of the heel angle of the yacht and the wind speed. It also discusses the corresponding optimal spanwise loading distributions. An extended lifting line code, based on Weissinger's method, is developed to analyze the performance of an isolated mainsail in upwind conditions. It is extended to account for the heel angle of the yacht via effective angle theory, and an image sail is used to model the influence of the sea surface. Profile drag is modeled using experimental data. The extended lifting line code is validated against wind-tunnel measurements and data from the literature. A second code is then used to optimize the spanwise loading on a mainsail such that the drive force is maximized. Constraints are implemented to ensure positive circulation over the entire span and to limit the sectional loading to realistic values. Finally, the extended lifting line code is inverted to calculate the twist distribution necessary to produce the desired, optimized loading distribution for a given sail planform. The calculated twist distribution is found to be realistic and achievable.

Nomenclature

a_k	=	Fourier coefficient for circulation series
b	=	span of sail or wing
C_{dp}	=	profile (friction + form) drag coefficient
C_l	=	sectional lift coefficient
D	=	drag
F_{drive}	=	drive force (parallel to yacht centerline)
F_{side}	=	side force (perpendicular to yacht centerline)
G	=	nondimensional circulation
h	=	footgap
L	=	lift
T	=	heeling moment
V_A	=	apparent wind speed
V_B	=	boat speed
V_{eff}	=	effective wind speed
V_T	=	true wind speed
V_∞	=	freestream velocity
w_i	=	induced downwash velocity
$w_{i,3/4}$	=	induced downwash velocity on 3/4 chord line
α	=	angle of attack
α_i	=	induced angle of attack
$\alpha_{L=0}$	=	zero-lift angle
β_A	=	apparent wind angle
β_{eff}	=	effective wind angle
Γ	=	circulation
γ	=	chordwise sail-bound vorticity
θ	=	heel angle
τ	=	twist angle of sail-chord relative to centerline of yacht
ϕ	=	angular coordinate describing spanwise position

Received 8 March 2010; revision received 16 May 2010; accepted for publication 17 May 2010. Copyright © 2010 by the American Institute of Aeronautics and Astronautics, Inc. All rights reserved. Copies of this paper may be made for personal or internal use, on condition that the copier pay the $10.00 per-copy fee to the Copyright Clearance Center, Inc., 222 Rosewood Drive, Danvers, MA 01923; include the code 0021-8669/10 and $10.00 in correspondence with the CCC.

*Graduate Student, Yacht Research Unit, Department of Mechanical Engineering. Currently, Postgraduate Student, Institute of Lightweight Design and Polymer Technologies, Technical University of Dresden, Germany.

†Postgraduate Student, Yacht Research Unit, Department of Mechanical Engineering, Private Bag 92019.

‡Associate Professor, Yacht Research Unit, Department of Mechanical Engineering, Private Bag 92019.

§Professor, Director Yacht Research Unit, Department of Mechanical Engineering, Private Bag 92019.

I. Introduction

IN PARTICULAR in the context of the America's Cup and the Volvo Ocean Race, the development of methods to analyze the flow around yacht sails has been pursued intensively. Since the late 1960s the attached flow around upwind sails has been studied with vortex lattice codes and boundary-layer methods [1,2]. Three decades later, computational methods based on the solution of the Reynolds-averaged Navier–Stokes equations (RANSE) saw their first practical application in sail design [3]. Today RANSE solvers are widely used to investigate separated flows around highly curved downwind sails like spinnakers, while relatively flat upwind sails, which exhibit large areas of attached flow, are normally designed with potential flow solvers. It is such an upwind sail with attached flow that is considered in this paper.

In recent years, research has mainly focused on the analysis problem of sail design, i.e., on finding the aerodynamic loads produced by a sail or by a combination of sails of given geometry. The *inverse problem* and the *optimization problem* have received far less attention. Following Labrujère and Sloof [4], who reviewed and classified computational methods for the aerodynamic design of aircraft components, the inverse problem is a problem in which the designer specifies an arbitrary pressure distribution on an airfoil or wing, while the geometry of the airfoil or the wing that realizes the given pressure distribution is determined as the result of the solution procedure. Aerodynamic optimization methods are those in which an optimization algorithm is linked with a flow analysis code to minimize or maximize an aerodynamic objective function such as the lift to drag ratio.

With aircraft wings, aerodynamic optimization is often split into two subproblems: The first problem is one of finding an optimal spanwise lift or circulation distribution (spanwise problem). In a second step one then needs to decide how to achieve this distribution by spreading out the circulation at a certain spanwise position along the chord (chordwise problem). In this paper, a similar approach is taken to optimize the performance of a yacht sail. The paper focuses on the optimization of the spanwise loading distribution. The corresponding chordwise problem is the subject of ongoing research and only partly considered here.

The optimization of the spanwise lift distribution of wings and similar lifting surfaces is often linked with minimization of the induced drag, which in turn leads to the well-known elliptical lift

Table 1 Differences between aircraft wings and sails

Typical wing	Sail
Operates in uniform freestream	Operates within the atmospheric boundary layer, which results in twisted incident flow.
Usually operates far from the ground	Operates a small distance away from the sea surface (footgap).
Can have more or less arbitrary planform	Physical limitations to the planform because it is made from flexible cloth. Additionally constrained by racing rules.
Made from metal, rigid construction with flaps and slats. Geometric twist is usually fixed.	Made from cloth; trimming sails changes shape of camber line, amount of geometric twist and also sail planform.
Usually fixed amount of dihedral and sweepback	The yacht is free to heel in response to moments applied by the sails and keel. This results in dihedral and sweepback that are a function of sail loading.
Operates in air only	Sail operates in air. Hull and the keel operate in water. This links the aerodynamics of an optimization for boat speed with the hydrodynamic characteristics of the hull.

distribution and a uniform downwash along the span. Jones [5] has shown that if additional constraints are added, such that for example the bending moment at the wing-fuselage junction is limited to a value below that obtained with elliptical loading then the constrained optimal lift distribution for the same total lift is one that gives rise to a downwash distribution, which varies linearly with span. While these basic ideas can be partially transferred to the study of upwind sails, there are many additional constraints and limitations that need to be considered, as described in Table 1.

In particular, the last two points in Table 1 make the optimization of sails more complicated than the optimization of wings. This is because an increase in lift produced by the sails will on the one hand increase the available drive force (i.e., the force component parallel to centerline of yacht); but on the other hand this will lead to an increased heeling moment and hence larger heel angles. Large heel angles in turn reduce the effective wind speed (perpendicular to the mast) and consequently all the aerodynamic forces decrease. Furthermore, large heel angles are usually associated with a loss of keel-efficiency and an increase of the hydrodynamic drag of the hull. While the ultimate goal will always be to maximize velocity made good to course (i.e., the component of the yacht's velocity in the direction of the next mark), simplified optimization objectives such as maximum drive force, minimum induced drag or minimum total drag of the sails have been suggested in an attempt to decouple the aerodynamics of the sails from the hydrodynamic characteristics of the hull.

Milgram [6] was the first to address the topic of optimal sail design. He used modified lifting line theory to minimize the induced drag of sails which produce a given amount of lift. In his numerical lifting line code, the headsail and the mainsail are represented by a lifting line each. The influence of the sea surface and the gap between the foot of the sails and the sea (the *footgap* from Fig. 1) is accounted for by the method of mirror images. Milgram expands the circulation distribution of each of the lifting lines in a Fourier sine-series. The heeling moment is reduced by an appropriate choice of the coefficients in the series. Profile drag is neglected in Milgram's optimization approach.

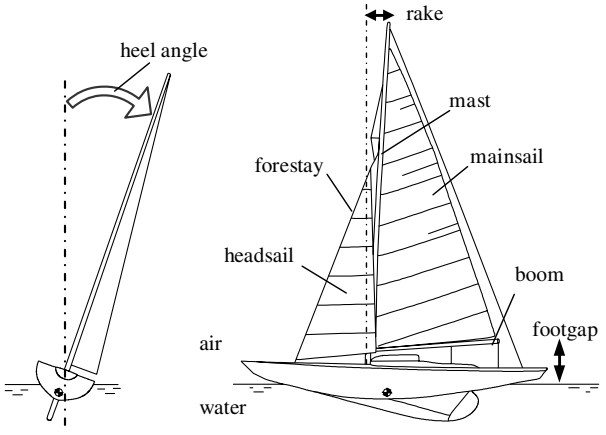

Fig. 1 Sailing terminology.

Sparenberg and Wiersma [7] and Wood and Tan [8] optimized the spanwise loading distribution for maximum drive force. While Wood and Tan placed a constraint on the heeling moment only, Sparenberg and Wiersma additionally placed a constraint on the heeling force. In both papers, headsail and mainsail are represented by a single, unheeled lifting line and its mirror image, and only induced drag is considered. For severe constraints on the heeling moment, the optimizations produced negative loading in the top section of the sails. Although this is a very effective way of maximizing the thrust of a sail while keeping the heeling moment below a certain value, sails that produce such an inverted loading (negative lift) near the head are impossible to build from cloth.

Greeley et al. [9] and Euerle and Greeley [10] also optimized for maximum drive force produced by the sails, placing a constraint on the maximum allowable heeling moment. The aerodynamic optimization is based on lifting line representations of the two sails. The sea surface and the footgap are again modeled by the method of mirror images. Because of the limitations of Prandtl's classical lifting line theory, mast rake and the angle between the vertical and the forestay (leading to sweepback in the lifting lines) are neglected. Profile drag and the influence of the mast on the flow around the mainsail are approximated by using experimentally derived sectional data. In the more recent paper, optimum spanwise circulation distributions are presented as a function of the heeling moment produced by the sails. Such an approach is not based on an actual balance between the aerodynamic heeling moment and the righting moment produced by the keel and the hull, and hence does not necessarily model the actual physics of sailing in moderate winds correctly.

Day [11] optimized sail plans for maximum velocity made good (i.e., the component of the yacht's velocity in the direction of the wind). Using the experimentally derived data of the Delft Systematic Yacht Hull Series [12], his approach also takes into account the hydrodynamic side of the optimization problem, i.e., the change in hull resistance with heel angle. The actual optimization is based on an evolutionary algorithm coupled to a vortex lattice code calculating the sail forces. Profile drag is accounted for by simply assuming constant values for form and skin friction drag. Results are presented in the form of the optimal sail planform for a particular yacht at a certain wind speed, thus little insight can be gained into the corresponding spanwise lift distribution. In another set of simulations, Day coupled the evolutionary algorithm to simple lifting line theory to maximize the speed of a surfboard, placing a constraint on the heeling moment. For this case, the results are also presented as spanwise circulation distributions. The results are similar to those obtained by Sparenberg and Wiersma [7] and Wood and Tan [8], i.e., the optimal circulation distributions exhibit an (impossible to realize) inverted loading near the head of the sail.

Recently optimization techniques based on evolutionary algorithms coupled to RANSE solvers saw their first applications in sail design. As shown by Casás et al. [13], such an approach can produce promising results, but being based on *brute force*, it requires significant computational resources and therefore does not seem to be suitable for preliminary design studies.

This paper presents a computationally inexpensive aerodynamic optimization for drive force based on an extended lifting line

representation of a mainsail. Only the case of an isolated mainsail (with no headsail present) is considered here. However, an extension of the theory to the case of two interacting sails is possible and is in fact the subject of ongoing research by the authors. Besides being more accurate than a standard (Prandtl) lifting line approach, an extended lifting line approach can also account for sweepback in the lifting line, i.e., for angled forestays or raked masts. Extended lifting line theory is based on the ideas of Weissinger [14] and can also be described as a vortex lattice method with a single chordwise panel. The aerodynamic model presented here accounts for the heel of the yacht, and an image sail is used to model the sea surface. Profile drag is predicted using experimental data from the literature. In the numerical optimization, the planetary boundary layer in which the yacht sails, and the resulting twist in the onset flow can be taken into account, and constraints are used to ensure positive circulation along the span, i.e., to avoid the unrealistic sail shapes in [7,8,11]. A simplified righting moment balance is used to model the interaction between drive force and heel angle, i.e., in the optimization the sail is free to heel in response to changes in the spanwise loading distribution. It is felt that such an approach models the reality of sailing better than the approach of placing a direct constraint on the heeling moment produced by the sail. Furthermore, such a righting moment balance facilitates a future incorporation of a model that determines the hydrodynamic drag based on the true heel angle of the yacht. The main goal of this paper is not so much to optimize the finer details of a sail, but to gain a better understanding of the behavior of the maximum drive force and corresponding optimal loading distributions as a function of heel angle and wind speed.

II. Methodical Approach

The paper is divided into three main sections that deal with: 1) performance analysis of America's Cup type mainsails, b) the optimization of the circulation distribution along the span of the sail, and c) the question of how to achieve the optimal loading distribution.

The performance analysis part (Sec. III) is based on an extended lifting line approach. The theory is then developed into a Matlab code taking into account the footgap under the sail, and geometric twist and camber distributions. Planform and configuration parameters such as rake and heel (corresponding to sweep and dihedral on a wing) are incorporated as well as experimental drag data. The performance analysis part of the paper is rounded off with the validation of the code against wind-tunnel measurements and data from the literature.

The next step is the inversion of the theory into an optimization. This is described in the optimization part of the paper (Sec. IV). Constant and nonlinear constraints are used in the optimization algorithm to restrict the solutions to those, which are physically valid and technically achievable.

The last part of the paper (Sec. V) addresses the question of how to achieve the optimal loading distribution. The results from this analysis are presented in the form of optimal geometrical twist distributions (trim) along the span of the sail. It is shown that a sail trimmed according to this trim guide will produce the loading distribution that corresponds to maximum drive force.

III. Sail Analysis Code

During an initial investigation of different methods to analyze the flow around a sail the idea of using Prandtl's classical lifting line theory was dismissed because it can overpredict the lift by up to 10% [15] and, more important, it cannot take account of mast rake, i.e., sweepback of the sail. Possible alternatives to classical lifting line theory are extended lifting line theory or vortex lattice codes. In the latter approach vortex elements and control points are usually located on the sail surface. Because the shape of the sail surface is not known in the optimization problem, the use of a vortex lattice code requires an iterative solution strategy leading to an increase in CPU-time. In spite of this drawback the development of such a method has been pursued by some of the authors and it was found that an inverse

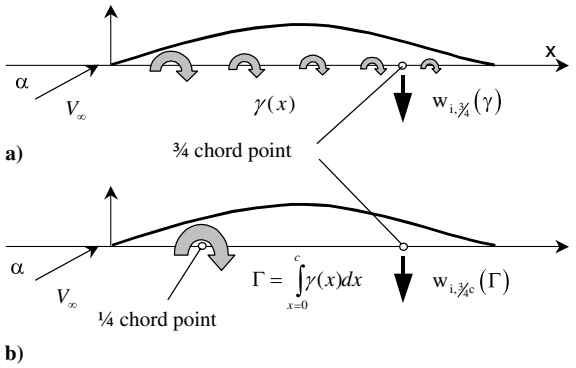

Fig. 2 Illustration of theorem of Pistolesi; a) continuous distribution of vorticity along the chord; b) discrete vortex of overall strength Γ placed on the quarter-chord point.

vortex lattice code produces very good results [16]. Although, not as accurate as a vortex lattice method extended lifting line theory has the advantage of being analytical in nature. This allows to directly calculate the sail shape or spanwise twist distribution that corresponds to a particular load distribution. For the present study it was therefore decided to use the extended lifting line approach of Weissinger [14] as a compromise between accuracy and computational effort.

A. Problem Formulation and Overview of Solution Procedure

In this paper the problem of finding the lift and drag produced by a sail of given geometry is tackled using Weissinger's approach [14], which is based on replacing the bound circulation by a vortex distribution on the quarter-chord, calculating the downwash on the three-quarter-chord and assuming that at this position the flow components normal to the sail vanish (tangential flow condition). The problem formulation of no normal flow at the three-quarter-chord line leads to an integro-differential equation. It is solved here by using a sine-series representation of the circulation that automatically fulfills the boundary conditions of zero circulation at the foot and the head of the sail. An adaptive Simpson-quadrature is used to compute the integrals appearing in the downwash equations. The solution of the resulting linear system of equations then yields the coefficients of the sine-series expansion of the circulation. Far-field analysis in the Trefftz-plane is finally used to determine the induced drag while the profile drag is accounted for semi-empirically.

B. Condition of Tangential Flow and the Theorem of Pistolesi

Weissinger [14] applies the theorem of Pistolesi to fulfill the boundary condition of tangential flow on the wing or sail surface. As summarized by Schlichting and Truckenbrodt [15], Pistolesi showed that for *circular arc* profiles, the continuous vorticity distribution along the chord produces the same amount of downwash at the three-quarter-chord point as a discrete vortex of same overall strength positioned at the quarter-chord point, see Fig. 2. Fulfilling the tangential flow condition at the 3/4-chord point then automatically enforces tangential flow *everywhere* on the (circular arc) camber. Consequently, the predicted sectional lift is in exact agreement with the continuous formulation according to thin airfoil theory. The advantage of this method is that the tangential flow condition needs to be fulfilled at a *single* point only.

Weissinger [14] accounts for the camberline shape by reducing the curved profile to an equivalent flat plate operating at an angle of attack of $\alpha = \alpha_{\text{geo}} - \alpha_{L=0}$, where α_{geo} is the geometrical angle of attack and $\alpha_{L=0}$ denotes the zero-lift angle of the profile. The latter angle can be calculated with thin airfoil theory and for profiles of the type sketched in Fig. 2, $\alpha_{L=0} < 0$. A flat plate operating at $\alpha = \alpha_{\text{geo}} - \alpha_{L=0}$ produces the same lift as the cambered airfoil at $\alpha = \alpha_{\text{geo}}$.

C. Vortex System Setup and Downwash Equation

Figure 3 illustrates the vortex system setup used to calculate the downwash at the three-quarter-chord line. The bound vorticity is represented by a vortex of strength $\Gamma(y)$ while the vortex wake is modeled as a planar vortex sheet, which has the direction of the incident flow. To fulfill the condition of tangential flow at the water surface, the concept of an image sail is used, i.e., a mirror image of the above vortex system is introduced.

As shown in the figure, a right-hand Cartesian coordinate system is introduced such that the positive x-direction points downstream and the y-direction points outward toward the tip of the sail. The y-direction is centered at half-span. Additionally, a dummy coordinate system ζ, η is introduced.

Using the Biot–Savart Law:

$$w_i = \frac{1}{4\pi}\int \frac{\Gamma \times r}{|r|^3}\,\mathrm{d}s \tag{1}$$

The downwash induced at point $P(x, y)$ becomes

$$w_i(x,y) = \text{sail}\begin{cases} -\int_{-b/2}^{b/2} \frac{(\mathrm{d}\Gamma/\mathrm{d}\eta)}{2\pi(y-\eta)}\cdot \mathrm{d}\eta \\ -\int_{-b/2}^{b/2} \frac{\Gamma(\eta)}{4\pi}\cdot\frac{(x-\zeta(\eta))+(\eta-y)\cdot\zeta(\eta)'}{((x-\zeta(\eta))^2+(y-\eta)^2)^{3/2}}\cdot \mathrm{d}\eta \\ -\int_{-b/2}^{b/2} \frac{(\mathrm{d}\Gamma/\mathrm{d}\eta)}{4\pi(y-\eta)}\left[\frac{x-\zeta(\eta)}{\sqrt{(x-\zeta(\eta))^2+(y-\eta)^2}}-1\right]\mathrm{d}\eta \end{cases}$$

$$\text{image}\begin{cases} +\int_{-b/2}^{b/2} \frac{(\mathrm{d}\Gamma/\mathrm{d}\eta)}{2\pi(y+\eta+2\cdot h+b)}\cdot \mathrm{d}\eta \\ +\int_{-b/2}^{b/2} \frac{\Gamma(\eta)}{4\pi}\frac{(x-\zeta(\eta))-(\eta+y+b+2h)\zeta(\eta)'}{((x-\zeta(\eta))^2+(y+\eta+b+2h)^2)^{3/2}}\,\mathrm{d}\eta \\ +\int_{-b/2}^{b/2}\left(\frac{(\mathrm{d}\Gamma/\mathrm{d}\eta)}{4\pi(y+\eta+2h+b)}\cdot\left[\frac{x-\zeta(\eta)}{\sqrt{(x-\zeta(\eta))^2+(y+\eta+2h+b)^2}}-1\right]\right)\mathrm{d}\eta \end{cases} \tag{2}$$

Without the sail-image terms, this equation has also been derived by Wickenheiser and Garcia [17] in the context of wing analysis. In the above expression, singularities in the terms for the trailing vortex sheet at $y = \eta$ have been removed by adding and subtracting the first term in the trailing vortex integral as suggested by DeYoung and Harper [18]. Although this singularity does not occur in the image sail integrals, the same procedure has been applied to produce similar terms that can be treated in an equivalent way in the solution procedure. Evaluating the downwash velocity on the three-quarter-chord line $x_{3/4c} = \zeta(y) + c(y)/2$ yields the downwash as a function of the spanwise coordinate only. Nondimensionalizing in the following way

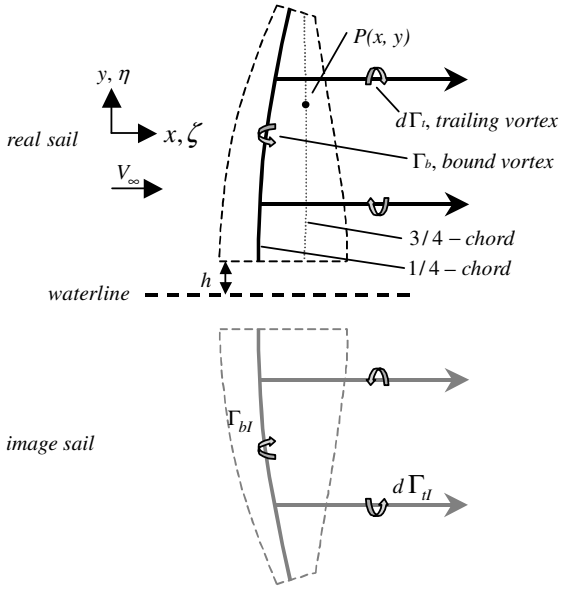

Fig. 3 Vortex system setup on sail and image.

$$\eta_n = \frac{\eta}{b/2},\qquad y_n = \frac{y}{b/2},\qquad G = \frac{\Gamma}{b/2\cdot V_\infty},\qquad x_n = \frac{\zeta}{c(y)}$$
$$\alpha_i = \frac{w_i}{V_\infty} \tag{3}$$

and transforming into angular coordinates using

$$\phi_v = \cos^{-1}(y_n)\quad\text{and}\quad \phi = \cos^{-1}(\eta_n) \tag{4}$$

results in the following expression for the downwash on the 3/4 chord line:

$$\begin{aligned} w_{i,3/4}/V_\infty = {} & \frac{1}{2\pi}\int_0^\pi \frac{-\partial G/\partial\phi}{(\cos(\phi)-\cos(\phi_v))}\cdot\mathrm{d}\phi \\ & + \frac{1}{2\pi}\int_\pi^0 \frac{\partial G/\partial\phi}{(\cos(\phi_v)+\cos(\phi)+\frac{2a}{b})}\,\mathrm{d}\phi \\ & + \frac{1}{4\pi}\left(\frac{b}{2c(\phi_v)}\right)^2\int_\pi^0 G(\phi)R(\phi_v,\phi)\sin(\phi)\,\mathrm{d}\phi \\ & - \frac{1}{4\pi}\left(\frac{b}{2c(\phi_v)}\right)^2\int_\pi^0 G(\phi)T(\phi_v,\phi)\sin(\phi)\,\mathrm{d}\phi \\ & - \frac{1}{4\pi}\int_\pi^0 (\partial G/\partial\phi)\cdot P(\phi_v,\phi)\cdot\mathrm{d}\phi \\ & + \frac{1}{4\pi}\int_\pi^0 (\partial G/\partial\phi)\cdot S(\phi_v,\phi)\cdot\mathrm{d}\phi \end{aligned} \tag{5}$$

where

$$P(\phi_v,\phi) = \frac{\Psi\cdot[\cos(\phi_v)-\cos(\phi)]^{-1}}{\sqrt{\Psi^2+\Omega^2[\cos(\phi_v)-\cos(\phi)]^2}} - \frac{1}{(\cos(\phi_v)-\cos(\phi))} \tag{6}$$

$$R(\phi_v,\phi) = \frac{\Psi + [\cos(\phi)-\cos(\phi_v)]\frac{\mathrm{d}x_n(\phi)}{\mathrm{d}\phi}}{\sqrt{\Psi^2+\Omega^2[\cos(\phi_v)-\cos(\phi)]^2}^3} \tag{7}$$

$$\begin{aligned} S(\phi_v,\phi) = {} & \left(\cos(\phi_v)+\cos(\phi)+\frac{2a}{b}\right)^{-1} \\ & \cdot\left(\frac{\Psi}{\sqrt{\Psi^2+\Omega^2(\cos(\phi_v)+\cos(\phi)+\frac{2a}{b})^2}}-1\right) \end{aligned} \tag{8}$$

$$\begin{aligned} T(\phi_v,\phi) = {} & \frac{\Psi}{\sqrt{\Psi^2+\Omega^2[\cos(\phi_v)+\cos(\phi)+\frac{2a}{b}]^2}^3} \\ & + \frac{(\cos(\phi)+\cos(\phi_v)+\frac{2a}{b})\frac{\mathrm{d}x_n}{\sin(\phi)\mathrm{d}\phi}}{\sqrt{\Psi^2+\Omega^2[\cos(\phi_v)+\cos(\phi)+\frac{2a}{b}]^2}^3} \end{aligned} \tag{9}$$

and:

$$\Psi = \Psi(\phi_v,\phi) = x_n(\phi_v) - x_n(\phi) + 1/2 \tag{10}$$

$$\Omega = \Omega(\phi_v) = b/(2c(\phi_v)) \tag{11}$$

It is now assumed that the dimensionless loading distribution can be represented by a Fourier sine-series. Such an ansatz function automatically enforces the boundary condition of zero circulation at the boom and the head of the sail. Thus

$$G(\phi) = \sum_{k=1}^{\infty} a_k\cdot\sin(k\phi) \tag{12}$$

with

$$a_k = \frac{2}{\pi}\int_0^{\pi} G(\phi)\sin(k\phi)\,\mathrm{d}\phi \tag{13}$$

and

$$G'(\phi) = \partial G/\partial\phi = \sum_{k=1}^{\infty} a_k \cdot k \cdot \cos(k\phi) \tag{14}$$

An exact integration method for the Fourier coefficients a_k is given by Multhopp's formula based on Gaussian quadrature [15]. However, a method more suitable for implementation on computers is used here, i.e., the Fourier coefficients are determined from the solution of Eq. (5) and then resubstituted into Eq. (12) to calculate the dimensionless circulation $G(\phi)$. Inserting Eqs. (12) and (14) into Eq. (5) and substituting

$$Q(\phi_v,\phi) = \frac{\cos(k\phi)}{(\cos(\phi_v)+\cos(\phi)+\frac{2\cdot a}{b})} \tag{15}$$

yields

$$\begin{aligned}\frac{w_{i,3/4}}{V_\infty} &= \frac{1}{2\pi}\sum_{k=1}^{\infty} k a_k \int_0^{\pi} \frac{-\cos(k\phi)}{(\cos(\phi)-\cos(\phi_v))}\,\mathrm{d}\phi \\ &+ \frac{1}{2\pi}\sum_{k=1}^{\infty} k a_k \int_{\pi}^{0} Q(\phi_v,\phi)\mathrm{d}\phi \\ &- \frac{1}{4\pi}\sum_{k=1}^{\infty} k a_k \int_{\pi}^{0} \cos(k\phi)P(\phi_v,\phi)\mathrm{d}\phi \\ &+ \frac{1}{4\pi}\sum_{k=1}^{\infty} k a_k \int_{\pi}^{0} \cos(k\phi)S(\phi_v,\phi)\mathrm{d}\phi \\ &+ \frac{1}{4\pi}\left(\frac{b}{2c(\phi_v)}\right)^2 \sum_{k=1}^{\infty} a_k \int_{\pi}^{0} \sin(k\phi)R(\phi_v,\phi)\sin(\phi)\,\mathrm{d}\phi \\ &- \frac{1}{4\pi}\left(\frac{b}{2c(\phi_v)}\right)^2 \sum_{k=1}^{\infty} a_k \int_{\pi}^{0} \sin(k\phi)T(\phi_v,\phi)\sin(\phi)\,\mathrm{d}\phi \end{aligned} \tag{16}$$

This is an expression for the downwash induced by the bound and trailing vortex system on the three-quarter-chord line and, as required by the theorem of Pistolesi, this downwash needs to cancel the upwash due to angle of attack and camber at the three-quarter-chord line

$$\underbrace{w_{i,3/4}(\phi)}_{\text{due to vortex system}} - \underbrace{V_\infty[\alpha_{\text{geo}}(\phi)-\alpha_{L=0}(\phi)]}_{\text{due to AOA and camber}} = 0 \tag{17}$$

Inserting Eq. (17) into Eq. (16) one finds that the only unknowns in Eq. (16) are the Fourier coefficients defining the loading distribution $G(\phi)$. Truncating the Fourier series for $G(\phi)$ after m terms and writing Eq. (16) at m positions along the span, i.e., at m angles ϕ_v, leads to an $m \times m$ system of linear equations for the unknown Fourier coefficients. This system can be solved using simple Gauss-elimination.

The first integral in Eq. (16) represents Glauert's integral and can be solved analytically. To the authors' knowledge, there exists no analytical solution for the remaining integrals in Eq. (16). The integrands of the remaining terms, are, however, smooth functions without diverging singularities; therefore, the integrals can be evaluated numerically using an adaptive Simpson quadrature as described in [19].

Once the Fourier coefficients a_k are known, the circulation distribution can be retrieved in y-coordinates with

$$\Gamma(y) = \frac{b}{2}\cdot V_\infty \cdot \sum_{k=1}^{m} a_k \cdot \sin\left(k\cos^{-1}\left(y\cdot\frac{2}{b}\right)\right) \tag{18}$$

This result is particularly useful because it gives the circulation distribution as a continuous, analytic function of the spanwise coordinate. The error of this solution depends on the number of Fourier coefficients used to approximate the circulation distribution and on the accuracy of the numerical integration, which in turn depends on the number of intervals, n, used in the integration. It can be shown that this error is proportional to the interval-length $t = (b-a)/n$ to the fifth power, $e \sim t^5 = [(b-a)/n]^5$, where the interval $[a, b]$ is divided into n subintervals. Although the integrands in Eq. (16) are rather complex, they are smooth, harmonic functions which the adaptive quadrature deals with very accurately. In the present case, n was usually in the order of 200 and the error is therefore negligible.

D. Derivation of Aerodynamic forces

1. *Lift and Induced Drag*

Once the circulation distribution is known the lift can be calculated from the Kutta–Joukowski theorem:

$$L = \rho_\infty \cdot V_\infty \int_{-b/2}^{b/2} \Gamma(y)\,\mathrm{d}y \tag{19}$$

Induced drag is calculated using far-field analysis in the Trefftz plane [17,20]

$$D_i = \rho_\infty \cdot V_\infty \int_{-b/2}^{b/2} \Gamma(y)\alpha_i(y)\,\mathrm{d}y \tag{20}$$

The induced angle of attack α_i in this expression can be calculated by taking half the limit of Eq. (2) as $x \to \infty$

$$\alpha_i(\phi_v) = \frac{w_i(\phi_v)}{U_\infty} = \frac{0.5}{U_\infty}\lim_{x\to\infty} w_i(x,y) \tag{21}$$

Transforming the resulting expression into angular coordinates and nondimensionalizing yields for the induced angle of attack:

$$\begin{aligned}\alpha_i(\phi_v) = &-\frac{1}{4}\sum_{k=1}^{m} k\cdot a_k \cdot \frac{\sin(k\phi_v)}{\sin(\phi_v)} + \frac{1}{4\pi}\sum_{k=1}^{m} k \\ &\cdot a_k \int_{\pi}^{0} \frac{\cos(k\phi)}{(\cos(\phi_v)+\cos(\phi)+\frac{2\cdot a}{b})}\,\mathrm{d}\phi\end{aligned} \tag{22}$$

The integral in this equation can be evaluated using an analytic expression given by Milgram [21]:

$$\int_0^{\pi} \frac{\cos(n\cdot\varphi)}{B-\cos(\varphi)}\,\mathrm{d}\varphi = \pi\cdot\frac{-1^{n+1}\cdot(|B|-\sqrt{B^2-1})^n}{\sqrt{B^2-1}} \tag{23}$$

Inserting Eq. (23) into Eq. (22) yields

$$\begin{aligned}\alpha_i(\phi_v) = &-\frac{1}{4}\sum_{k=1}^{m} k\cdot a_k \cdot \frac{\sin(k\phi_v)}{\sin(\phi_v)} + \frac{1}{4}\sum_{k=1}^{m} k\cdot a_k \\ &\cdot \frac{-1^{n+1}\cdot(|B|-\sqrt{B^2-1})^n}{\sqrt{B^2-1}}\end{aligned} \tag{24}$$

where

$$B = -\cos(\phi_v) - \frac{2\cdot a}{b} \tag{25}$$

This is a closed-form representation of the induced angle of attack distribution and can be used in Eq. (20) to compute the induced drag D_i. The integration in Eq. (20) is performed using numerical trapeze integration. The number of control points in this integration is independent of the number of Fourier coefficients and can be chosen very high to avoid introducing additional errors in the computation of the induced drag.

2. *Profile Drag*

According to the widely used International Measurement System sail force model summarized in [22] profile drag can account for more than 20% of the total drag of the sails when sailing upwind and

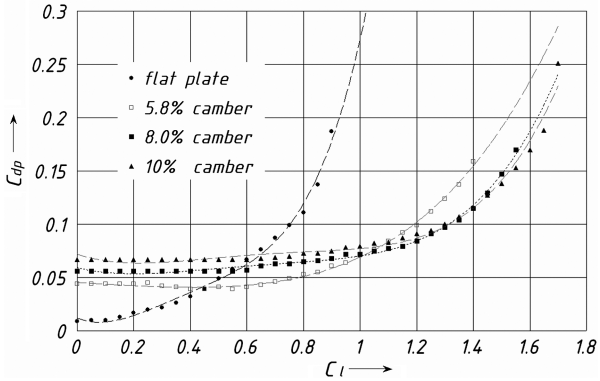

Fig. 4 Profile drag of sail sections after Dayman [23].

therefore needs to be taken into account when analyzing the aerodynamic forces. In this paper, sectional drag data from experiments by Dayman [23] at a Reynolds number of $Re = 400,000$ were used to account for the profile drag of the sail sections. The drag data were tabulated as a function of camber and lift coefficient and interpolated over the required range. The sectional profile drag coefficient as a function of lift coefficient was approximated with a polynomial of degree four

$$c_{dp} = f_0 + f_1 \cdot c_l + f_2 \cdot c_l^2 + f_3 \cdot c_l^3 + f_4 \cdot c_l^4 \tag{26}$$

The sectional drag data of Dayman and the corresponding polynomial fits are shown in Fig. 4.

3. Aerodynamic Drive and Side Forces

As illustrated in Fig. 5 drive force (i.e., the aerodynamic force component parallel to the centerline of the yacht) and side force (perpendicular to the centerline) for an upright yacht can be obtained by resolving the lift and drag into a yacht-fixed coordinate system

$$\begin{bmatrix} F_{\text{drive}} \\ F_{\text{side}} \end{bmatrix}_{\text{boat}} = \begin{bmatrix} \sin(\beta_A) & -\cos(\beta_A) \\ \cos(\beta_A) & \sin(\beta_A) \end{bmatrix} \cdot \begin{bmatrix} L \\ D \end{bmatrix}^{xy} \tag{27}$$

where β_A is the *apparent wind angle*, i.e., the angle between the centerline of the yacht and the apparent wind. The apparent wind in turn results from the vector addition of true wind speed V_T and the boat speed V_B, as illustrated by the *apparent wind triangle* in Fig. 5.

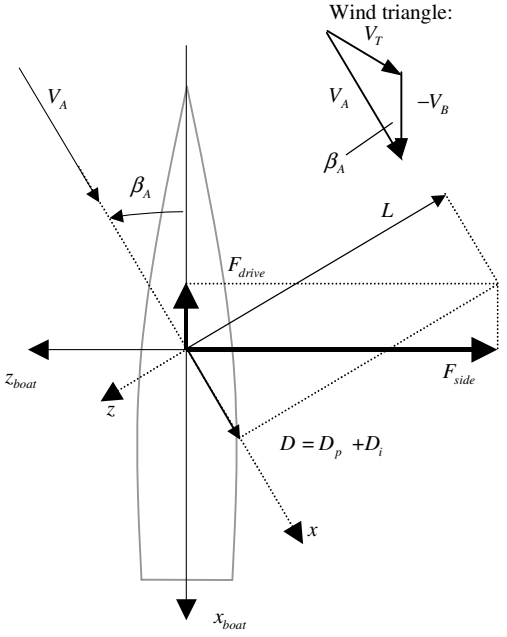

Fig. 5 Aerodynamic forces acting on an upright yacht as seen from above.

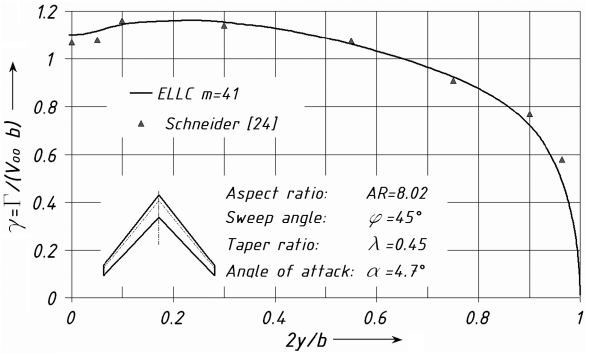

Fig. 6 Theoretical and measured circulation distributions as function of half-span.

E. Results from Extended Lifting Line Sail Analysis and Code Validation

The sail-analysis code was validated against data from the aeronautical literature as well as against results from wind-tunnel tests with a sail model.

1. Verification Using Data from the Literature

Figure 6 shows the nondimensional circulation distribution along the span of a sweptback wing of aspect ratio 8.2 as measured by Schneider [24]. Schneider obtained this distribution by evaluating pressure measurements from wind-tunnel tests at $Re = 4 \cdot 10^6$. Also shown in the figure is the circulation distribution for the same sweptback wing as predicted by the extended lifting line code (ELLC). As can be seen, the agreement between predicted and measured distributions is excellent. In particular the drop of the circulation at the wing root is modeled satisfactorily. The ELLC predictions in the graph are based on approximating the circulation distribution with $m = 41$ terms in the Fourier series. The figure shows that the difference between ELLC predictions and Schneider's data is in the order of $\pm 2\%$ over 90% of the span. When integrating the circulation distributions over the span to calculate the lift, the error reduces further and becomes negligible.

Figure 7 shows a test case for a wing of much smaller aspect ratio (AR = 2.75). The symbols represent theoretical data from Schlichting and Truckenbrodt [15], while the lines correspond to the predictions from the ELLC. The agreement between the ELLC predictions and the results from [15] is very good.

In the ELLC, the equation of the quarter-chord-line needs to be a continuous analytical function. In both of the above test cases, the kinked quarter-chord-line was approximated using a series expansion for the absolute value function [25]

$$x_n(y_n) = \frac{a \cdot 8}{c \cdot \pi^2} \sum_1^n \frac{-1^{\left(\frac{n-1}{2}\right)}}{n^2} \cdot \sin\left(\frac{\pi}{2} n(y_n + 1)\right) + a \quad \text{with:}$$

$$a = \tan(\varphi) \cdot b/2 \tag{28}$$

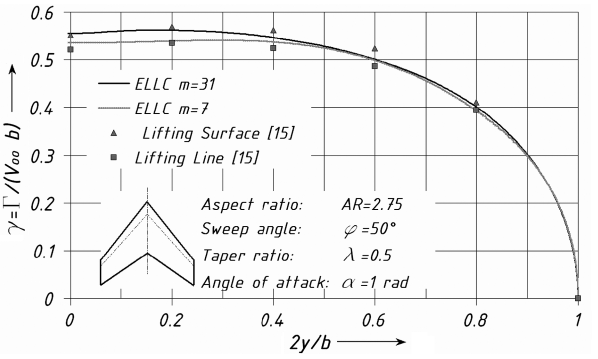

Fig. 7 Comparison of various theoretical circulation distributions as function of half-span.

where $b/2$ is the half-span and φ the sweep angle. Using $n = 60$ terms in this sine-series expansion yields good results for the kink in the root sections of the wings.

2. *Validation against Wind-Tunnel Measurements*

The above results show that the loading distribution of sweptback, tapered and low aspect ratio aircraft wings can be accurately modeled with the ELLC. A sail, however, operates near the sea surface and this is modeled in the ELLC via an image sail. To validate this approach, tests were carried out at the Twisted Flow Wind Tunnel of The University of Auckland. This open test section, open return tunnel was specifically developed for testing yacht sails [26]. The current tests were performed using a 1:17 scale rigid fiberglass model of an America's Cup 90 (AC90) rule mainsail suspended from wires. Aerodynamic forces in uniform, untwisted flow were measured by means of a six-component force balance underneath the wind-tunnel floor using the procedure detailed in [27]. The setup is shown in Fig. 8.

Aerodynamic forces produced by the support frame were determined in separate test runs without the sail model present and subsequently subtracted off the force values recorded with the sail present.

In a pretest the variations in freestream dynamic pressure with height within the sail frame was found to be in the order of 1 Pa at a mean of 60 Pa (10 m/s), corresponding to a relative difference of 1.5%. All sail measurements were performed at a wind speed of 8 m/s for medium angles of attack and 5 m/s at higher angles of attack because the load cells of the force balance reached their limit at the higher wind speed. The Reynolds numbers where based on the average chord length of $c_{\text{avg}} = 0.49$ m and were $Re_{8\text{ m/s}} = 260,000$ and $Re_{5\text{ m/s}} = 164,000$, respectively.

Figure 9 shows the results of the measurements in the form of lift coefficient plotted as function of the boom angle of attack. i.e., the angle of attack at the foot of the sail. The fact that the sail exhibits a large geometric twist of 14.4° over the span results in negative incidence angles in the top sections if the boom angle of attack is less than 14.4°. As can be seen from the figure, below an angle of attack of 15° the lift increases linearly with angle of attack because the flow is attached over most parts of the sail span. At angles above 15°, the lift curve slope drops off due to an increased amount of separation occurring at the foot of the sail. In the experiments, this was observed with the aid of wool tufts.

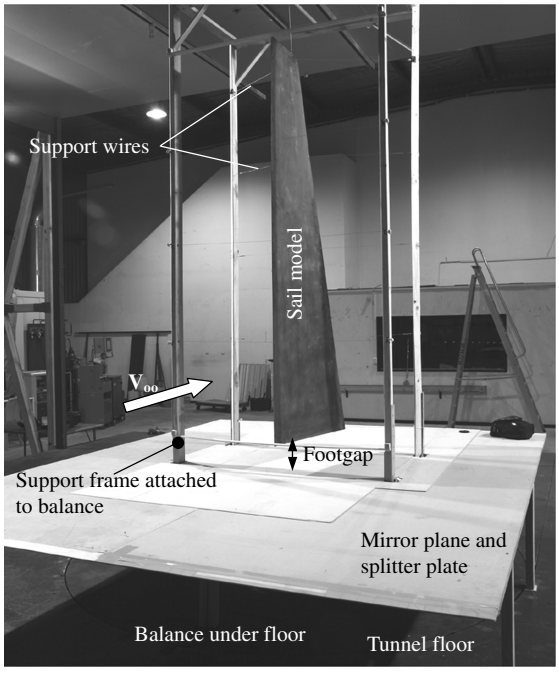

Fig. 8 Sail attachment and rig setup in the Twisted Flow Wind Tunnel.

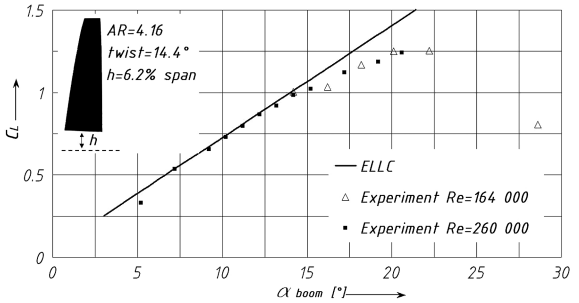

Fig. 9 Lift coefficient as function of boom angle of attack. Comparison between theory and measurements.

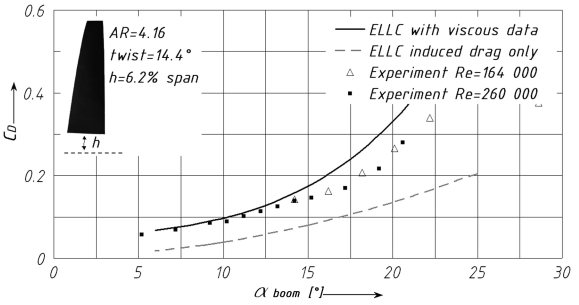

Fig. 10 Drag coefficient as function of boom angle of attack. Comparison between theory and measurements.

In summary it can be said that the ELLC predicts the slope of the lift polar accurately and represents the experimental results to within 2% in the linear part of the lift curve. This range extends from very low boom angles of attack up to around 14° boom angle of attack. This also indicates that the effect of the footgap is modeled correctly. In actual sailing, the sail will have a smaller angle of attack than 14° even in close-hauled upwind conditions as the flow is turned by the headsail. At very low boom angles of attack, which correspond to a negative incidence in the top sections of the sail, the prediction is still accurate to within 2% of the experimental results. However, at angles of attack between 15 and 20°, the sectional lift slope of 2π used in the ELLC overpredicts the sail performance by about 10%.

Figure 10 shows the corresponding results for the drag coefficient (with and without the profile drag data from Dayman [23]) as a function of boom angle of attack.

At boom angles of attack between 7 and 14°, the drag prediction is good and within 10% of the experimental results. At higher angles, the drag prediction actually overestimates the drag found in the experimental analysis of the AC90 mainsail. One possible explanation for this can be the sparlike leading and trailing edge supports used by Dayman. It is quite likely that these spars increase the amount of flow separation on the sails at high angles of attack and that the drag measured by Dayman is therefore higher than what was measured in the Twisted Flow Wind Tunnel where no spars were used. Nevertheless, including the empirical drag data leads to a significant improvement over the prediction of induced drag by finite wing theory only. It can be seen that the profile drag is of the same order of magnitude as the induced drag and therefore needs to be taken into account in any computer program aiming to optimizing the spanwise loading distribution.

IV. Optimization of Spanwise Lift Distribution

A. Problem Formulation and Overview of Solution Procedure

In this section, the spanwise circulation of a sail of representative geometry at a fixed apparent wind angle ($\beta_A = 17°$) and with a fixed and realistic footgap of $h = 5.7\%$ of the span is optimized to yield maximum drive force. Effective angle theory is used to account for reduction of aerodynamic forces with heel. This theory is based on the idea of ignoring any mast-parallel velocity components of the

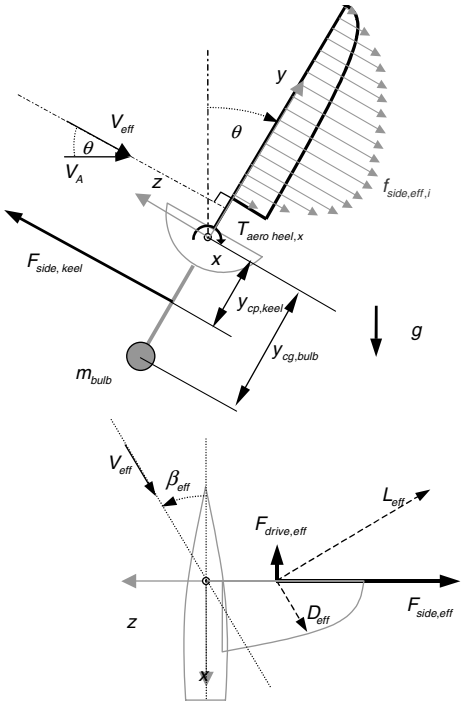

Fig. 11 Forces and moments acting on a heeled yacht.

incident velocity V_A (see Fig. 11), i.e., it is assumed that only mast-normal velocity component V_{eff} produces lift and drag. The flow in the heeled plane is called the effective flow and is defined by the effective wind angle β_{eff} and the effective wind speed V_{eff}, which can be calculated from the apparent wind angle β_A and the heel angle θ as follows [27]:

$$\beta_{\text{eff}} = \tan^{-1}(\tan(\beta_A) \cdot \cos(\theta)) \tag{29}$$

$$V_{\text{eff}} = V_A \cdot \sqrt{1 - \sin^2(\beta_A) \cdot \sin^2(\theta)} \tag{30}$$

In the optimization, a simplified righting moment balance is used to simulate how a yacht heels in response to changes in the spanwise loading distribution. This righting moment balance is described in Sec. IV.B. Furthermore, the sectional lift is bounded by a lower limit of zero circulation and an upper limit determined by $c_{l,\max}$ as a function of camber, derived from Dayman [23]. Optimal loading distributions are calculated under varying conditions. They are discussed in terms of sailing conditions and sail trim. The mathematical formulation of the optimization procedure can be summarized as

$$\max_{\Gamma_i} F_{\text{drive}} \quad \text{subject to} \sum T_x(\theta = \text{const.}) = 0 \qquad \Gamma_i \geq 0$$
$$\Gamma_i \leq 0.5 \cdot V_{\text{eff},i} \cdot c_{l,\max} \cdot c_i \tag{31}$$

where the drive force and moment balance are formulated in terms of the discretized circulation strengths at i spanwise stations $\Gamma_i (i = 1 \ldots n)$, see also [19].

A nonlinear optimization method implemented in Matlab is used to find an optimum distribution of the Γ_i's to produce the maximum drive force under the given nonlinear constraints.

The drive force and heeling moment contributions from a sail section at height y_i can be expressed as

$$f_{\text{drive}}(y_i) = \Delta y \cdot [-\sin(\beta_{\text{eff}}) \cdot l_{\text{eff}}(y_i) + \cos(\beta_{\text{eff}}) \cdot d_{\text{eff},i}(y_i) + \cos(\beta_{\text{eff}}) \cdot d_{\text{eff},fp}(y_i)] \tag{32}$$

$$t_{\text{aero,heel},x}(y_i) = \Delta y \cdot [\cos(\beta_{\text{eff}}) \cdot l_{\text{eff}}(y_i) \cdot y_{\text{ref},i} + \sin(\beta_{\text{eff}}) \cdot d_{\text{eff},i}(y_i) \cdot y_{\text{ref},i} + \sin(\beta_{\text{eff}}) \cdot d_{\text{eff},fp}(y_i) \cdot y_{\text{ref},i}] \tag{33}$$

and the total drive force and heeling moment developed by the sail is given by

$$F_{\text{drive}} = \sum_{i=1}^{n} f_{\text{drive}}(y_i) \tag{34}$$

$$T_{\text{aero,heel}} = \sum_{i=1}^{n} t_{\text{heel}}(y_i) \tag{35}$$

wherein Δy represents the constant spanwise element width, n the number of evaluation points over the span, and y_{ref} the sectional lever-arm about the heel axis (yacht-axis), d_i is the drag contribution from induced velocities on the sail and d_p is the profile drag and l the lift. The profile drag is accounted for by using a fourth-order polynomial fit to the experimental data of Dayman. The lift in Eqs. (32) and (33) is expressed in terms of Γ using the Kutta–Joukowski theorem. The induced drag is calculated with the sectional formulation of Eq. (20).

The solution of the optimization procedure defined in Eq. (31) can then be performed at a fixed wind speed and heel angle. The result is the spanwise circulation distribution that leads to maximum drive force and the value of this drive force. To produce an output that is comparable to the one of the analysis code, a Fourier sine-series can be fitted to the optimization results for the circulation strengths Γ_1 to Γ_n. It was found that numerical smoothing had to be applied to the boundary elements to avoid oscillations [19]. This method proved to be successful in the range of calculations performed.

B. Heeling Moment Balance

Figure 11 illustrates the simplified heeling moment balance used in the optimization to account for the interaction between aerodynamic forces and moments and heel angle. The heeling axis is assumed to lie on the waterline. In order for the boat to be sailing at a constant heel angle, these forces and moments need to be in balance, thus

$$\sum T_x = 0 = m_{\text{bulb}} g y_{cg,\text{bulb}} \sin(\theta) - F_{\text{side,keel}} y_{cp,\text{keel}} - T_{\text{aero},x} \tag{36}$$

Herein, the side force produced by the keel $F_{\text{side,keel}}$ needs to be equal but opposite to the sail side force $F_{\text{side,eff}}$ to balance the forces in y and z-directions. Thus

$$\sum T_x = 0 = m_{\text{bulb}} g y_{cg,\text{bulb}} \sin(\theta) + F_{\text{side,eff}} y_{cp,\text{keel}} - T_{\text{aero},x} \tag{37}$$

In this paper the geometrical dimensions and masses that appear in this equation were taken from the America's Cup 90 Class Rule Version 1.0 [28]. To ensure a realistic moment constraint for the simulation of an isolated mainsail the keel bulb mass was scaled by the ratio of mainsail lift to genoa lift based on data from Larsson and Eliasson [22].

C. Results of Spanwise Loading Optimization and Discussion

1. *Drive Force Surfaces*

In the following the results from the optimization of the spanwise loading distribution are presented as surface plots illustrating the maximum drive force as function of heel angle and apparent wind speed. The drive force surfaces shown are limited to a range of apparent wind speeds and heel angles, which can be expected in upwind sailing for an AC90 yacht. The sailing conditions in an America's Cup race are regulated by the racing rules and are usually in the limit of 8–25 kts of true wind speed. For a given apparent wind angle, here $\beta_A = 17°$, the apparent wind speed V_A can be

calculated based on the performance of earlier America's Cup yachts by analyzing the ratio of true wind speed V_T to boat speed V_B, see also apparent wind triangle in Fig. 5. The apparent wind speed seen on the yacht then ranges from around 16–35 kts (8–18 m/s) for the above-mentioned range of true wind speeds. The upper limit on the heel angle was set to 30°. This limit is common during upwind legs of America's Cup races. Figure 12 shows a dimensional drive force surface from an optimization run that did not include profile drag.

For fixed wind speeds, the maximum drive force is predicted to increase if the heel angle is increased. The same behavior is predicted for constant heel angle but increasing wind speed. Consequently, the point of sailing corresponding to maximum drive is predicted to be at the limiting heel angle of 30° and the highest apparent wind speed used in the calculation. This result is a consequence of the low drag penalty imposed on the optimization routine by solely including induced drag. To sail at a fixed heel angle at higher wind speeds, the sail needs to be depowered and the center of effort lowered and the upper sections of the sail will therefore fly at a very low lift coefficient, which in turn reduces the induced drag. The induced drag goes to zero as the sail lift coefficient approaches zero, and no penalty is imposed on the drive force due to low lift but high drag, which would be the case when including profile drag.

The results from the optimizations that also include profile drag are shown in Fig. 13. The drive force surface for this case differs significantly from the one in Fig. 12. Quantitatively, a reduction in the predicted optimum drive force by 50% may be noticed for high apparent wind speeds. More important, the shape of the drive force surface has changed and the maximum drive force no longer occurs at the highest wind speeds. In the low-speed range, increasing the heel angle initially yields an increase in maximum drive force. However, beyond a critical heel angle, which itself is a function of speed, the maximum drive force decreases. At higher wind speeds, the maximum in drive force shifts toward higher heel angles until it is essentially cut off by the heel angle limit placed at 30°. At very high wind speeds, the maximum drive force is predicted to occur at the limiting heel angle.

As far as the decrease in drive force beyond a certain critical heel angle is concerned the predictions closely represent the behavior of sail forces as experienced in real-life sailing. The predicted decrease in maximum drive force for high wind speeds beyond the point of globally optimum drive force is an interesting result and would make a good topic for future investigations.

The effects of twist and shear in the incident flow were analyzed in additional optimization runs. Wind twist and shear introduce a certain amount of vorticity in the onset flow and, strictly speaking, lifting line theory cannot be used to analyze sails in such a rotational onset flow. However, Euerle and Greeley [10] have shown that, in upwind conditions, the twist over the height of the sail is small and that potential flow solvers will predict the sail lift and drag in an adequate manner. As the results from the optimizations that include twist and shear do not differ significantly from the results in Fig. 13 they are not presented here.

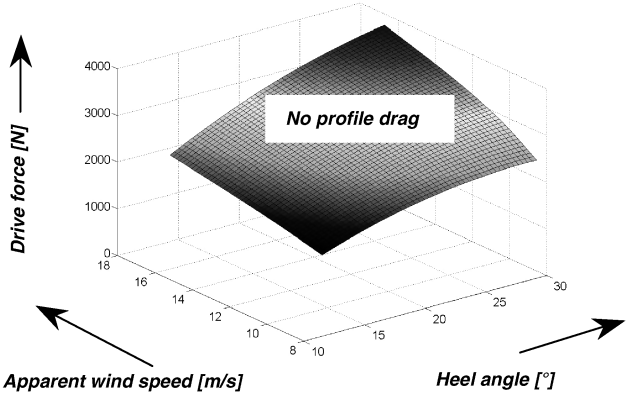

Fig. 12 Drive force surface in from optimization that accounts for induced drag only, $\beta_A = 17°$.

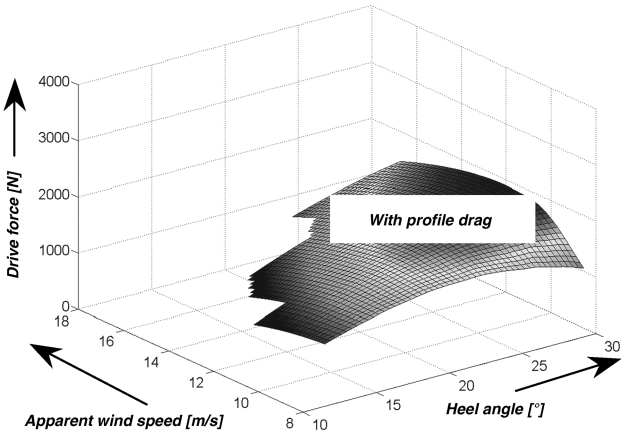

Fig. 13 Drive force surface from optimization that accounts for induced drag and profile drag, $\beta_A = 17°$.

2. Loading Distributions for Maximum Drive Force

Each point on the above drive force surfaces corresponds to the optimum drive force at a particular combination of wind speed and heel angle. Using the results from the optimization routine the spanwise loading distribution for each of the points on the surface can be determined. Considering a constant wind speed of, e.g., $V_{A,\mathrm{ref}} = 8.3$ m/s i.e., slicing through the drive force surface from Fig. 13 at this wind speed and plotting the optimum loading distribution corresponding to the drive force at each heel angle yields the solid lines in Fig. 14.

It becomes evident that, at low wind speeds and high heel angles (i.e., no limit on the heeling moment), the distribution becomes essentially elliptical, which is the well-known result for minimum induced drag. The sail will be highly loaded in these cases to produce a heeling moment strong enough to heel the yacht to the desired heeling angle. In terms of induced drag, this sailing condition is very efficient; however, the profile drag penalty becomes very large when the sections approach their maximum lift coefficient (see Fig. 4) and eventually cause a reduction in drive force for very high heel angles, see Fig. 13. If the heel angle is limited to smaller values, the sail lift needs to be reduced, which corresponds to a smaller area under the loading curve. The most efficient way to do this in terms of the drive force is by shifting the maximum in the distribution toward the boom and hence downward, i.e., by lowering the center of effort height of the sail.

Also shown in Fig. 14 are optimum loading distributions for a higher apparent wind speed of $V_{A,\mathrm{ref}} = 14.4$ m/s (dashed lines). As can be seen from the shape of the resulting curves, the additional constraint of positive circulation along the span is now active near the top of the sail and ensures distributions that are achievable with a cloth sail. From the shape of the curves it becomes obvious that, to sail at low heel angles, the optimization routine depowers the top sections of the sail (i.e., these sections do not produce lift at all). This

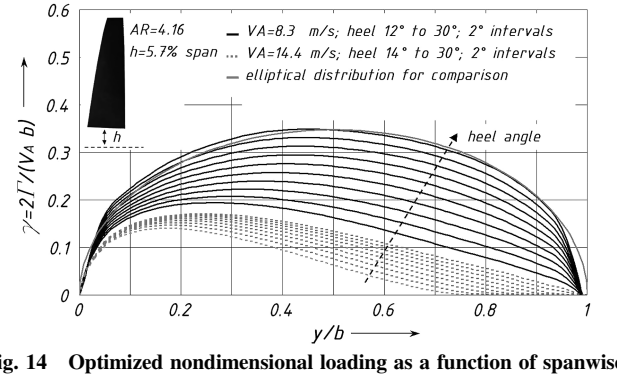

Fig. 14 Optimized nondimensional loading as a function of spanwise coordinate and heel angle for two apparent wind speeds $V_A = 8.3$ m/s and $V_A = 14.4$ m/s. Apparent wind angle $\beta_A = 17°$.

result compares well to how one would trim the mainsail of a real yacht in stronger winds.

V. Sail Trim Guide

This section deals with part of the question how to actually achieve optimal loading distributions of the type shown in Fig. 14. A certain sectional circulation can be achieved in a number of different ways, i.e., by changing the local chord length, by changing the amount or position of maximum camber (i.e., the zero-lift angle) or by changing the geometric twist. As mentioned in the introduction, this chordwise problem of finding the *best* way of producing the circulation distributions from Fig. 14 is still the subject of ongoing research. Only the simple way of influencing the circulation distribution by changing the twist distribution is considered here.

By simply inverting the analytical sail analysis code from Sec. III, one can calculate the geometric sail twist needed to obtain a certain spanwise circulation distribution. The optimized loading distribution for an apparent wind speed of $V_A = 10$ m/s, an apparent wind angle of $\beta_A = 17°$ and a heel angle of $\theta = 26°$ is used here to derive the sail trim (i.e., the geometric twist) that would be required to achieve the desired loading with the AC90 mainsail and a realistic footgap of 5.7% of the span. The raw results of such a sail trim calculation are shown in Fig. 15 (triangular symbols). Trimming a real cloth sail to such an irregular distribution is impossible. A linear twist distribution, however, seems to be achievable, and a linear function was therefore fitted to the optimized twist points using a least-squares approach. The outliers at the foot and the head were ignored, because the outer sections do not contribute significantly to the loading distribution.

This linear distribution is also shown in Fig. 15 (dashed line). It is defined by a boom sheeting angle of 9.8° and a sheeting angle of 14.8° at the head of the sail. The resulting 5° twist over the span is realistic and achievable with a cloth sail.

Figure 16 finally shows the resulting loading distributions. In this figure the triangular symbols represent the output of the optimization routine, i.e., the original target distribution that will lead to the largest possible drive force at $V_A = 10$ m/s, $\beta_A = 17°$ and $\theta = 26°$. The continuous distribution in the figure was calculated with the extended lifting line sail analysis code from Sec. III and is based on the linearized, least-squares fit shown in Fig. 15. The close agreement between the optimized loading (target) and the loading predicted for the linear twist distribution proves the consistency of the codes developed. Also shown in the figure is the circulation distribution that would be obtained if the nonlinear twist distribution in Fig. 15 could be realized. As can be seen, the difference between the three distributions is very small and it can hence be concluded that trimming the AC 90 sail to the linear twist distribution will result in a circulation distribution that is very similar to the optimized target distribution. It can be expected that, within the limitations of extended lifting line theory, a sail trimmed in such a way will deliver the largest possible drive force for the assumed conditions.

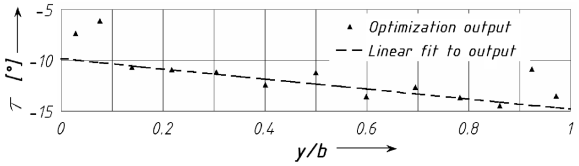

Fig. 15 Optimized sectional trim angle τ between local chord and centerline of yacht as function of spanwise location. $V_A = 10$ m/s, $\beta_A = 17°$, $\theta = 26°$ and $h = 5.7\%$.

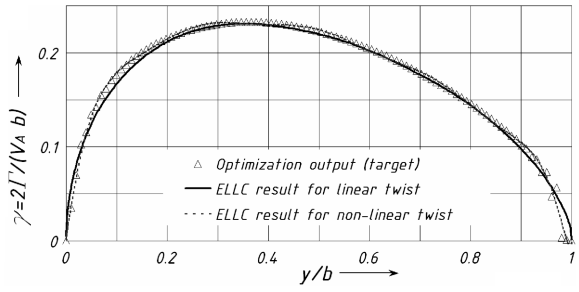

Fig. 16 Optimized spanwise load distributions. Comparison between optimized target distributions and output of ELLC.

VI. Conclusions

This paper deals with the topic of maximizing the drive force of an isolated upwind sail using extended lifting line theory and nonlinear optimization techniques.

Extended lifting line theory (Weissinger's 3/4 chord point method) is computationally very inexpensive and, as opposed to standard lifting line theory, it can take rake of the mast (i.e., sweepback) into account. In the present study the influence of the sea surface is modeled using the usual method of an image sail and profile drag is modeled based on experimental, sectional data. Results from wind-tunnel tests indicate that extended lifting line theory predicts the lift and drag of an upwind sail with attached flow to within 2 and 10%, respectively.

As an analysis tool the advantage of the Weissinger method lies in its simplicity and speed. Therefore, the developed code could be a useful tool to analyze sail shapes and the resulting lift and drag forces in real-time on the water. With regard to an optimization of sail shapes the advantage of the developed method over, for example, a vortex lattice code is the *analytical* nature of the theory. This makes it possible to *directly* calculate the sail shape or spanwise twist distribution that corresponds to a particular optimized load distribution.

In the second part of the paper the drive force (force parallel to centerline of yacht) produced by a mainsail is maximized using a nonlinear optimization approach. Results from this optimization can be presented in the form of surface plots showing the maximum drive force as a function of the heel angle of the yacht and the wind speed. A surface plot from optimization runs that ignore profile (i.e., viscous) drag indicates that the highest drive force always occurs at the maximum permissible heel angle of the yacht. More realistic calculations that also include profile drag show more than a 50% reduction in attainable drive force compared with the inviscid case. More important, the shape of the drive force surface changes, and for lower wind speeds the maximum drive force no longer occurs at the largest heel angle. This behavior is caused by the profile drag penalty of highly loaded sail sections verging on separation and closely resembles the behavior of the sail forces as experienced on a real yacht.

An analysis of the spanwise loading distributions behind the drive force surfaces shows that, for low wind speeds and large heel angles, the optimal lift distribution is essentially elliptical, whereas for higher wind speeds and small heel angles the center of effort needs to be lowered by shifting the maximum of the lift distribution towards the boom. This theoretical result closely reflects the practice of *twisting off* the head of the sail when sailing in stronger winds.

The question of how to achieve the optimized loading distribution for a specific wind speed is also addressed. By simply inverting the analytical theory developed in the first part of the paper, the analysis code becomes a design code. This code is used to determine the sail geometry (in this case the twist distribution) that corresponds to the optimized loading distribution. It is found that a linear distribution can produce the desired loading. For the analyzed sample case the resulting twist of the sail is about 5° over the span, which seems to be realistic and achievable.

Acknowledgments

The first author acknowledges the support of Michael Casey, Head of the Institute of Thermal Turbo-Machinery at the University of Stuttgart. All authors thank Emirates Team New Zealand for providing the AC90 sail geometry.

References

[1] Milgram, J., "The Analytical Design of Yacht Sails," *Transactions of the Society of Naval Architects and Marine Engineers*, Vol. 95, 1968, pp. 118–152.

[2] Norris, S. E., "The Interaction of Yacht Sails in a Two-Dimensional Viscid Flow," ME Thesis, Mechanical Engineering Department, Univ. of Auckland, Auckland, New Zealand, 1993.

[3] Jones, P., and Korpus, R., "International America's Cup Class Yacht Design Using Viscous Flow CFD," *The 15th Chesapeake Sailing Yacht Symposium*, Society of Naval Architects and Marine Engineers, Annapolis, MD, 2001, pp. 27–34.

[4] Labrujère, T. E., and Slooff, J. W., "Computational Methods for the Design of Aircraft Components," *Annual Review of Fluid Mechanics*, Vol. 25, 1993, pp. 183–214.

[5] Jones, R. T., "The Spanwise Distribution of Lift for Minimum Induced Drag of Wings Having a Given Lift and a Given Bending Moment," NACA TN 2249, 1950.

[6] Milgram, J. H., "Sailing Vessels and Sails," *Annual Review of Fluid Mechanics*, Vol. 4, 1972, pp. 397–430. doi:10.1146/annurev.fl.04.010172.002145

[7] Sparenberg, J. A., and Wiersma, A. K., "On the Maximum Thrust of Sails by Sailing Close to Wind," *Journal of Ship Research*, Vol. 20, No. 2, 1976, pp. 98–106.

[8] Wood, C. J., and Tan, S. H., "Towards an Optimum Yacht Sail," *Journal of Fluid Mechanics*, Vol. 85, No. 3, 1978, pp. 459–477. doi:10.1017/S0022112078000749

[9] Greeley, D. S., Kirkman, K. L., Drew, A. L., and Cross-Whiter, J. H., "Scientific Sail Shape Design," *The 9th Chesapeake Sailing Yacht Symposium*, Annapolis, MD, 1989, pp. 33–80.

[10] Euerle, S. E., and Greely, D. S., "Towards a Rational Upwind Sail Model for VPPs," *The 11th Chesapeake Sailing Yacht Symposium*, Society of Naval Architects and Marine Engineers, Annapolis, MD, 1993, pp. 75–86.

[11] Day, A. H., "Sail Optimisation for Maximal Speed," *Journal of Wind Engineering and Industrial Aerodynamics*, Vol. 63, No. 1–3, 1996, pp. 131–154. doi:10.1016/S0167-6105(96)00073-6

[12] Gerritsma, J., Onnink, R., and Versluis, A., "Geometry, Resistance and Stability of the Delft Systematic Yacht Hull Series," *International shipbuilding progress*, Vol. 28, No. 328, 1981, pp. 276–297.

[13] Casás, V. D., Peña, F. L., and Duro, R. J., "Exploring Automatic Evolutionary Yacht Sail Design," *3rd High Performance Yacht Design Conference*, The Royal Institution of Naval Architects, Auckland, New Zealand, 2008, pp. 82–90.

[14] Weissinger, J., "The Lift Distribution of Swept-Back Wings," NACA TM 1120, 1947.

[15] Schlichting, H., and Truckenbrodt, E., *Aeorodynamik des Flugzeuges*, 3rd ed., Springer, Heidelberg, 2001.

[16] Pilate, J. P., Gerhardt, F. C., and Flay, R. G. J., "A Three-Dimensional Inverse Sail Design Method," *International Journal of Small Craft Technology*, (to be published).

[17] Wickenheiser, A. W., and Garcia, E., "Aerodynamic Modelling of Morphing Wings Using an Extended Lifting-Line Analysis," *Journal of Aircraft*, Vol. 44, No. 1, 2007, pp. 10–16. doi:10.2514/1.18323

[18] DeYoung, J., and Harper, W., "Theoretical Symmetric Span Loading for Wings Having Arbitrary Planform," NACA TR 921, 1948.

[19] Junge, T. "Inverse Design of Optimal Sails," ME Thesis, Department of Mechanical Engineering., Univ. of Stuttgart, Stuttgart, Germany, 2009.

[20] Munk, M. M., "The Minimum Induced Drag of Airfoils," NACA TR 121, 1921.

[21] Milgram, J., "The Design and Construction of Yacht Sails," M.Sc. Thesis, Naval Architecture and Marine Engineering Dept., Massachusetts Inst. of Technology, Cambridge, MA, 1962.

[22] Larsson, L., and Eliasson, R., *Principles of Yacht Design*, 2nd ed., Adlard Coles Nautical, London, 2000.

[23] Dayman, B., "Experimental Aerodynamics of a Two-Dimensional Sail," M.Sc. Thesis, California Inst. of Technology, Pasadena, CA, 1953.

[24] Schneider, W. C., "A Comparison of the Spanwise Loading Calculated by Various Methods with Experimental Loadings Obtained on a 45° Sweptback Wing of Aspect Ratio 8.02 at a Reynolds Number of 4×106," NACA TR 1208, 1952.

[25] Stöcker, H., *Taschenbuch Mathematischer Formeln und Moderner Verfahren*, Harri Deutsch, Frankfurt, 1992.

[26] Flay, R. G. J., "A Twisted Flow Wind Tunnel for Testing Yacht Sails," *Journal of Wind Engineering and Industrial Aerodynamics*, Vol. 63, 1996, pp. 171–182. doi:10.1016/S0167-6105(96)00080-3

[27] Hansen, H., "Enhanced Wind Tunnel Techniques and Aerodynamic Force Models for Sail Yachts," Ph.D. Dissertation, Mechanical Engineering Department, University of Auckland, Auckland, New Zealand, 2006.

[28] America's Cup 90 Class Rule, Version 1.0 (2009), Issued by America's Cup Management, S. A., 2007.